Ultrasonics 114 (2021) 106403

Contents lists available at ScienceDirect

Ultrasonics

journal homepage: www.elsevier.com/locate/ultras

Discrimination of nano-objects via cluster analysis techniques applied to time-resolved thermo-acoustic microscopy

Andrea Ronchi [a,b,c], Andrea Sterzi [d], Marco Gandolfi [e,f], Ali Belarouci [g], Claudio Giannetti [b,c], Natalia Del Fatti [h], Francesco Banfi [b,h,*], Gabriele Ferrini [b,c,*]

[a] Department of Physics and Astronomy, KU Leuven, Celestijnenlaan 200D, 3001 Leuven, Belgium
[b] Interdisciplinary Laboratories for Advanced Materials Physics (I-LAMP), Università Cattolica del Sacro Cuore, I-25121 Brescia, Italy
[c] Dipartimento di Matematica e Fisica, Università Cattolica del Sacro Cuore, I-25121 Brescia, Italy
[d] Empa, Swiss Federal Laboratories for Materials Science and Technology Überlandstrasse 129, 8600 Dübendorf, Switzerland
[e] CNR-INO, Via Branze 45, 25123 Brescia, Italy
[f] Department of Information Engineering, University of Brescia, Via Branze 38, 25123 Brescia, Italy
[g] Institut des Nanotechnologies de Lyon - CNRS - Ecole Centrale de Lyon, 36 Avenue Guy de Collongue, 69134 Ecully, France
[h] FemtoNanoOptics group, Université de Lyon, Institut Lumière Matière (ILM), Université Lyon 1 and CNRS, 10 rue Ada Byron, 69622 Villeurbanne cedex, France

ARTICLE INFO

Keywords:
Photothermics
Photoacoustics
Microscopy
Cluster-analysis
Non-destructive testing
Single metal nano-object
Nanometrology

ABSTRACT

Time-effective, unsupervised clustering techniques are exploited to discriminate nanometric metal disks patterned on a dielectric substrate. The discrimination relies on cluster analysis applied to time-resolved optical traces obtained from thermo-acoustic microscopy based on asynchronous optical sampling. The analysis aims to recognize similarities among nanopatterned disks and to cluster them accordingly. Each cluster is characterized by a fingerprint time-resolved trace, synthesizing the common features of the thermo-acoustics response of the composing elements. The protocol is robust and widely applicable, not relying on any specific knowledge of the physical mechanisms involved. The present route constitutes an alternative diagnostic tool for on-chip non-destructive testing of individual nano-objects.

1. Introduction

Nanofabrication is one of the mainstays of modern technology and metallic nano-objects are important building blocks, used in various technological contexts. For instance, metallic nanoparticles synthesized by laser ablation [1–3] or gas-phase deposition [4–6] are emerging as useful materials in a variety of fields. Functionalized gold nanoparticles [7,8] are extensively used in technological areas spanning from novel optical biosensors [9], distribution of drugs to diseased organs [10,11], photothermal cancer treatment[12,13], new mass sensors [14]. In this context, patterned metallic nanostructures or lithographed on dielectric or conductive surfaces are particularly relevant, finding applications across a wide variety of fields such as electronics and microsystems, medical and biotech devices, optics and photonics, environment and energy harvesting applications [15–17].

As a consequence of their widespread use, it is important to develop fast, reliable, and unsupervised methods to sort out problems in nano-manufacturing [18,19] such as the inspection of the production uniformity and the detection of outliers, i.e. defect control. The primary inspection tools for nano-objects are the set of available well-established microscopy techniques, that proved invaluable to study metallic nanoparticles in different environments and nanostructures in general [20]. Ultrafast optical methods have recently emerged as competitive techniques for nanometrological inspection of devices [21–29]. However, there are situations where established techniques may not be the best choice for the tasks outlined above.

For instance, optical microscopy techniques [30,31] recently allowed to discriminate morphological features of nominally identical nanopatterned samples of subwavelength dimensions. Morphological information was ultimately retrieved implementing standard FEM simulations of the electromagnetic problem at hand while varying the samples' geometric parameters, until simulated features, similar to the experimental ones, were obtained [32]. However, this procedure is extremely time-consuming, needs to be readapted to each specific sample geometry/composition and it requires constant operator supervision together with a very fine knowledge of the sample itself to start

* Corresponding authors.
E-mail addresses: francesco.banfi@univ-lyon1.fr (F. Banfi), gabriele.ferrini@unicatt.it (G. Ferrini).

https://doi.org/10.1016/j.ultras.2021.106403
Received 30 September 2020; Received in revised form 7 February 2021; Accepted 11 February 2021
Available online 28 February 2021

with. Hence, this technique is not suited as a diagnostic tool in a production environment. Furthermore, also the higher resolution electron microscopies, such as Transmission Electron Microscopy (TEM) or Scanning Electron Microscopy (SEM) [20], are not suited for rapid and nondestructive sample imaging. The former is an inherently destructive technique, while the latter is affected by image distortion due to emitted secondary electrons when operating on an undoped dielectric substrate due to surface charging. Moreover, both techniques require working in a vacuum environment. Atomic force microscopy (AFM) [33] has reached scanning speed enabling, for instance, the imaging of proteins at video rates. However, AFM does not allow accessing encapsulated nanostructures and the nanostructure interface with the substrate. Summarizing, the above-mentioned microscopies, although serving as invaluable tools for a one-time inspection of a sample morphological feature, may not be the best suited for the rapid inspection of nanostructures in an industrial environment.

Cluster analysis is an unsupervised method that could be applied to Time-Resolved Thermo-Acoustic Microscopy (TR-TAM), in order to overcome the limitations of established microscopies and complement them [34,35]. To this aim, we here propose a discrimination technique based on TR-TAM and data mining techniques [36].

In many real-world applications, the nano-objects details and the environment characteristics are not known and a complete characterization is not required. When a manufacturing process fails or delivers nano-objects with characteristics different from the expected standard, the clustering analysis presented in this work may constitute a proper choice to isolate the outliers. As an example of this general issue, we focus on discriminating similar, nominally circular, metallic nanodisks nanopatterned on a dielectric substrate. Such a system is paradigmatic for a variety of applications ranging from plasmonics nano-resonators, nano-acoustic transducers, and whatever circular building block exploited in nanocircuitry.

We will focus on the optical investigation of a *single* nanostructure. However, the clustering is not achieved by measuring a single characteristic of the traces (e.g. the nanodisks acoustical and thermal kinetics as discussed below) but considering the differences/similarities among all the traces at once. In addition to being more robust, this analysis allows us to quantitatively retrieve average values for the clusters in a meaningful way, not normally achieved by single trace fitting, where the association of a trace to a cluster is a difficult choice when dealing with very similar traces. It is important to note that the global analysis of traces of single nanostructures gives more information than an analysis of traces averaged in experiments (e.g. a spectroscopic trace obtained from polydispersed nanostructures measured with a single laser spot) because in this case the outliers can be clearly identified and removed, thus avoiding to distort average values and failing to represent meaningful data.

The investigation is conducted by two-color infrared ASynchronous OPtical Sampling (ASOPS) pump–probe microscopy [37,38] on two sets of gold nanodisks of nominal diameters 90 and 100 nm, respectivley, deposited on a sapphire substrate, see Fig. 1. Since the excitation is in the infrared, the response from the gold nanostructures does not involve plasmonic resonances [32]. The technique is thus widely applicable, allowing us to choose the light wavelength to optimize, for example, the penetration into the host matrix and reduce scattering in turbid media. The ASOPS technique allows rapid scanning of the pump and probe delay, reducing drastically the time needed for a single measurement and simplifying the optical set-up, especially when coupled to optical microscopy. The time-delay is controlled electronically thus avoiding any moving mechanical stage. On one side, this grants superior stability of the optical beams with respect to the sample, on the other, an higher acquisition speed [39].

The signals obtained from the pump–probe experiments entail information on the relaxation of the energy injected in the nanodisk, in the form of an exponential decay (of both electron and thermal energy pathways) of the differential transmission of the probe beam. The mechanical (acoustic) oscillations, are superposed as a modulation on the decaying exponential [40,39]. The investigation is based on the optical excitation of different nanodisks structures and their discrimination based only on their optical response. The time-resolved spectra will be analyzed using two approaches: a hierarchical binary cluster tree dendrogram built using a euclidean distance (Ward Method) [41] and the singular value decomposition (SVD) analysis [42]. The hierarchical cluster analysis is usually adopted to discover relationships in data, the SVD has many useful applications in signal processing [43] and statistics.

2. Experimental

The laser system used in this work, based on the ASynchronous OPtical Sampling (ASOPS) technique [37,38], is coupled to a microscope to perform single-nanoparticle pump–probe experiments, see Fig. 1(a), (b). Briefly, the system is composed of two fiber lasers with wavelengths of 780 nm (probe) and 1560 nm (pump) that emit pulses with a time width of about 150 fs at a 100 MHz repetition rate. The probe laser repetition rate is detuned with respect to the pump laser. Because of the detuning, a mutual temporal delay between the pump and the probe pulse is accumulated. The high intensity pump beam excites the sample and the probe beam, with lower intensity, captures the dynamic of the sample at a varying delay. The probe laser beam does

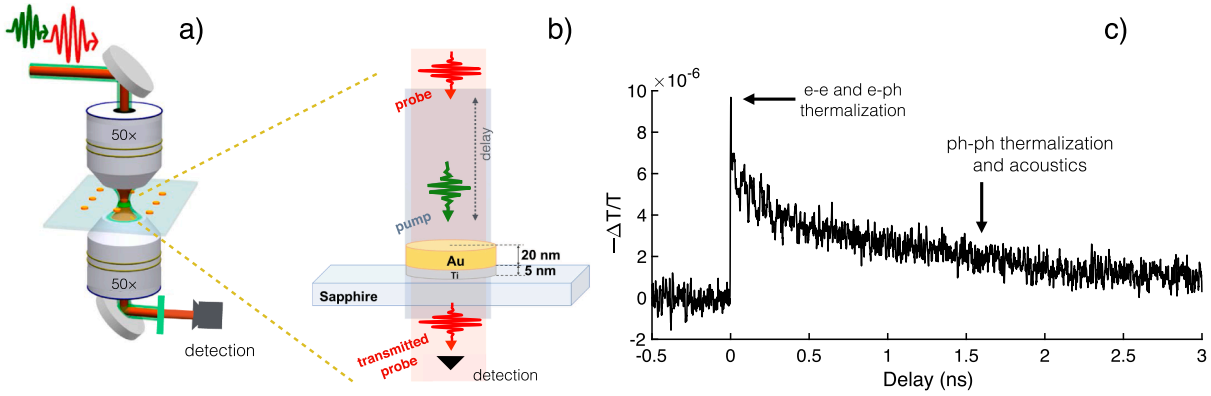

Fig. 1. (a) Single-nanoparticle time-resolved optical microscopy technique. Pump (green) and probe (red) beams are tightly focused on a single nanodisk via a high numerical aperture objective. The transmitted beams are collected by an opposing objective identical to the focusing objective, only the probe beam is measured. (b) A close-up view of the single nanodisk with the sample geometrical structure and thickness. The nominal diameters varies and are 90 nm and 100 nm, respectively. (c) A typical time-resolved trace on a nanodisk evidencing the fast electron–electron and electron–phonon initial relaxation, the slower thermalization with the substrate and the oscillation due to the mechanical excitation of the nanodisk.

not substantially modify the optical response of the sample. In this way, the entire relaxation dynamic of the single-nanodisk sample is measured, Fig. 1(c). The all-electronic management of the temporal delay between the two laser pulses eliminates the problems that characterize the traditional pump–probe method. With traditional techniques, the maximum delay range is of the order of 1–3 ns without specialized efforts. Using the ASOPS technique, the temporal delay window is increased normally by one order of magnitude, up to 10 ns.

The microscope is constituted by a focusing 50× long working distance objective with 0.55 NA, a sample scanning stage with few nm resolution, and a collecting objective identical to the focusing objective for the transmitted probe beam, Fig. 1(a). The beam sizes are shaped with telescopes before entering the focusing objective, the beam average power controlled via a half-waveplate – polarizer combination. The pump and probe beams enter the focusing objective collinearly and interact with the sample at normal incidence. The measured pump FWHM diameter is 2.4 μm, the probe FWHM diameter is 1.0 μm. No effort was made to achieve diffraction limited laser spot sizes, to keep the set-up as simple as possible in view of an on-line deployment for chip inspection. The typical pump fluence is 13 mJ/cm^2, the probe fluence is 0.5 mJ/cm^2. The probe beam emerging from the collecting objective is injected via a parabolic mirror into an optical fiber and guided to a differential photodiode. The differential photodiode is balanced with a reference beam in the absence of the pump and measures the pump induced variation in the probe beam transmitted power. Knowing the average beam power, it is possible to measure the relative transmission variation induced by the pump pulse. A typical time-resolved experimental trace is shown in Fig. 1(c).

The sample substrate was divided in two sections, where, respectively, disks with nominal diameters of 90 nm and 100 nm were nano-patterned via standard Electron Beam Lithography. The nanodisks consist of 20 nm-thick Au adhering, via a 5 nm Ti adhesion layer, to a monocrystalline sapphire substrate (Al_2O_3) (R-plane cut, size 10 mm × 10 mm and thickness of 127 μm), Fig. 1(b). The sapphire plate has the merit to be a transparent dielectric in the near infrared (refractive index 1.76 @ 780 nm and 1.74 @ 1560 nm [44]) with thermal conductivity $k = 30$ Wm^{-1}K^{-1} @ 300 K [45]. The choice of a transparent medium with a high k implies increasing the thermal diffusivity and allows us to consider the sapphire "almost" isothermal during the heat exchange process between nanodisk and substrate [6,46].

Here, we stress that both the nanodisks thickness and the diameters reported are nominal ones, so much as the fact that the disks are cylinders. As a matter of fact, upon AFM and SEM inspections, diameter deviations of the order of 10% and non-flat cylinder tops have been observed throughout the sample. The nanodisks might also be affected by deviations from a circular top-view with varying degrees of ellipticity. More specifically similar deviations have recently been reported on nano-patterned nanodisks with nominal diameters smaller than 100 nm [32]. These aspects arise due to the complicacy entailed in performing e-beam lithography on insulating substrates when designing sub 100 nm highly symmetrical features. Furthermore, electrons scattering occurring within the e-beam resist exposes unwanted regions of the resist itself. This fact may lead to strong relative deviations with respect to the nominal pattern upon size reduction. In this respect, "90 nm diameter" or "100 nm diameter" should be considered as labels referring to batches from separate manufacturing processes. The present sample thus constitutes an ideal system to evaluate alternative diagnostic tool for on-chip non-destructive testing of individual nano-objects.

3. Results and discussion

We identify three different temporal dynamics, corresponding to three different time scales as well documented in the literature [47,46]. Initially, the pump pulse excites the nanodisk, which absorbs an energy density U. The absorbed energy produces the heating of the electron gas of the metallic nanostructure in a sub-picosecond time scale. Successively, the electrons thermalize with the lattice's phonons through scattering processes on a picosecond time scale. The effect is an increase of the lattice temperature Θ to $\Theta + \Delta\Theta$, which causes thermal expansion of the nanostructure. As a result of these processes, we measure a decrease of the beam transmitted power induced by the pump pulse. Finally, the thermal energy accumulated in the disk relaxes toward the substrate on a nanosecond time scale. In this step, the energy density U absorbed by the nano-objects is transferred to the substrate in the form of mechanical and thermal excitations [48].

To investigate the dynamics outlined above, we measure the probe differential transmission, defined as $\Delta T/T = (P(on,\tau) - P(off))/P(off)$, where $P(on,\tau)$ is the average probe power measured by a photodetector at a fixed delay time τ from the pump pulse, $P(off)$ is the average probe power in the absence of the pump.

As the dissipating processes take place, the nanostructure slowly returns to its thermo-mechanical equilibrium. The differential probe transmission $\Delta T/T$ tends to zero as the disk thermalizes with the substrate. Together with the typical exponential decay, an oscillation in the relative transmittance $\Delta T/T$, due to the launching of an acoustic (mechanical) mode in the nanostructure, is observed.

In Fig. 2(a) we show all the experimental traces that will be analyzed below. The traces are smoothed to reduce the high-frequency noise. Each trace is measured on different individual Au nanodisks of nominal sizes 100 nm (5 disks) and 90 nm (4 disks), then normalized to the maximum absolute value. The numbering of the traces will be used in the subsequent analysis. In the following, we concentrate on long temporal dynamics and have left out from the fitting analysis the sub-ps peak near delay zero, which has been studied in the literature [47] and does not convey much information for our purposes. Each curve has been fitted with a double decaying exponential (colored lines). The exponentials are characterized by two distinct decay times. A slow decay time of the order of 2 ns and a fast decay time of the order of 200 ps. To analyze the acoustical frequencies, the residuals of the fit to each trace are Fourier transformed, shown in Fig. 2(b). In each Fourier spectrum, we note two main peaks, the highest in magnitude around 15–20 GHz (frequency f_1) and a secondary peak in the region 9–12 GHz (frequency f_2). The main peak in each frequency region is highlighted with a mark and the numerical value of the frequency in GHz.

To rationalize these frequencies, we made a finite element model (FEM) of the gold nanodisk, the titanium adhesion layer and the sapphire substrate (see supporting information (SI), Section 1 and Fig. 1 for details). The mechanical resonances of the nanodisk were identified by applying isotropic stress at a varying frequency and quantifying the stored mechanical energy. The stored energy versus frequency maxima allows to identify the resonances of the mechanical system (see Fig. 2 in SI). The calculated resonant frequencies for disks whose nominal diameter varies from 90 nm to 100 nm are in the 15–20 GHz range accessed in experiments. However, the simulations do not show any resonance peak in the 9–12 GHz, as seen in the experiments. To justify those low-lying frequencies, a 2 nm thick transition layer has been added between the adhesion titanium layer and the substrate to model the interface properties responsible of the disk adhesion. The transition layer mechanical properties are obtained as a weighted average of those of Ti and Poly(methyl methacrylate) (PMMA). The presence of PMMA is justified as a spurious addition during the deposition process. When the transition layer PMMA filling factor, defined as the PMMA percentage content entering the transition layer, approach unity, the model shows low-lying mechanical resonances in the 9–12 GHz range (see Fig. 3 in SI). For further details refer to SI, Section 1.

3.1. Hierarchical clustering

The dynamics measured on the disks with different dimensions are similar, the signature of the specific time-response residing in tiny

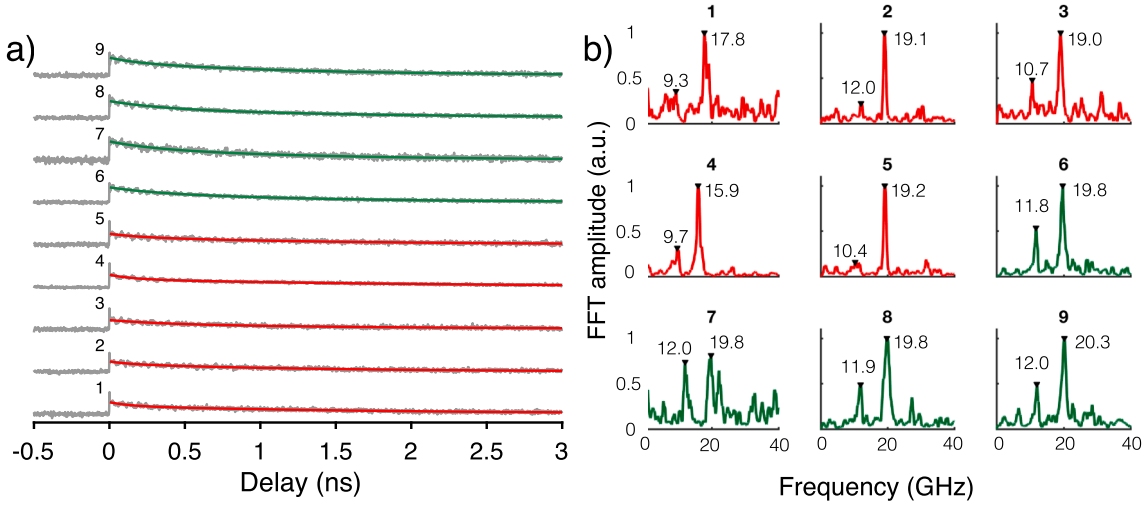

Fig. 2. (a) Differential transmission versus time delay measured on single nano-disks. The curves have been normalized with respect to the maximum absolute value and have been restricted to a temporal range up to 3 ns. The colored lines are double-exponential fits to the data (in gray). Red lines: 100 nm diameter single-nanodisk. Green lines: 90 nm diameter single-nanodisk. (b) Fourier transform of the residuals obtained from the fitting procedure, with the same numbering and color codes. The black marks highlight the prominent peaks in the frequency regions 9–12 GHz and 15–20 GHz. The numerical values of the peak frequencies are reported in GHz.

differences. It is important to note that the traces are affected by noise fluctuations superposed on the exponential decay dynamic due to the different experimental conditions (temperature, humidity, laser fluctuations, etc.). In this section, we discriminate the traces using a dendrogram through a hierarchical clustering principle. A dendrogram is a tree diagram frequently used to illustrate clusters produced by hierarchical clustering obtained using algorithms known as linkage rules. We have used a linkage rule known as "Ward's minimum variance method" [41]. This method has been used extensively in marketing, linguistics, biomedical and geospatial research, much less in physics and nanotechnology. Ward's method clusters data with the criterion to minimize the total within-cluster sum of squares (or variance) of the Euclidean distances between the objects in the cluster and its centroid. For a technical description, see the SI, Section 2.

The results of hierarchical clustering applied directly to the experimental traces in Fig. 2 a) are presented in the linkage plot and dendrogram shown in Fig. 3. In this case, each trace is interpreted as a point in a highly dimensional *trace space*, with many dimensions D = 3145. The data form two clusters. Each cluster is associated with a different nanodisk's diameter.

Besides the traces themselves, hierarchical clustering applies to the parameters that result from a fitting procedure. We fit these traces using a linear combination of two decaying exponentials (4 fit parameters: two amplitudes, two decay times), leaving out the initial fast peak due to the electronic response. Successively, a linear combination of two damped cosines at different frequencies (8 fit parameters: two amplitudes, two damping times, two frequencies, two phases) fit the residuals of the two decaying exponentials. We organize the fitting parameters of each trace in a 12 × 9 matrix *F*. See SI Section 3 for more details and Section 3.2 for fitting results. Since the fitting parameters are heterogeneous, to avoid the dependence of distances in the *parameter space* from the choice of dimension units, the rows of *F* have been normalized to zero average and unit standard deviation. The results of hierarchical clustering applied to the normalized parameters matrix *F* are shown in the linkage plot and dendrogram in Fig. 4. The data form two distinct clusters, each associated with one nanodisk's diameter. The parameter space has much lower dimensions (D = 12) than the trace space. In both analyses, hierarchical clustering reveals the internal similarities in data, discriminating time-resolved optical traces from objects in the 100 nm range differing in dimension by 10%.

The dimensional reduction, however, requires a physical model to derive the fit functions. It is important to note that this is an unsupervised clustering algorithm, particularly appropriate for automatic analysis. Once set a threshold to discriminate clusters (usually in terms of a percentage of the maximum linkage distance), the algorithm automatically identifies them. Specific labeling of the traces is not necessary.

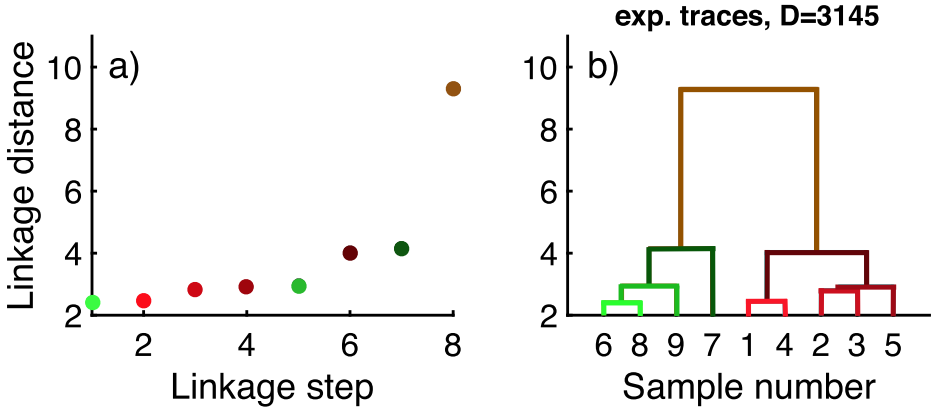

Fig. 3. Hierarchical cluster analysis of the trace space. (a) Linkage distance for each clustering step. (b) Dendrogram obtained using the Ward method. The vertical lengths between nodes are proportional to the linkage distance. Shades of red: 100 nm gold nanodisks. Shades of green: 90 nm gold nanodisks.

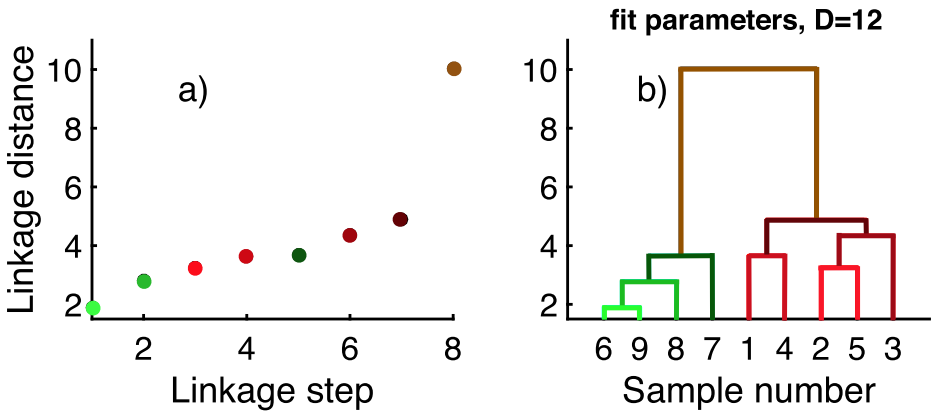

Fig. 4. Hierarchical cluster analysis of the fit parameter space. (a) Linkage distance for each clustering step. (b) Dendrogram obtained using the Ward method. The vertical lengths between nodes are proportional to the linkage distance. Shades of red: 100 nm gold nanodisks. Shades of green: 90 nm gold nanodisks.

We use knowledge of labels *a posteriori to prove that the algorithm discriminates correctly*.

3.2. Singular value decomposition

We organize the experimental traces as columns of a $m \times n$ data matrix X. Rows (m) map the delay time, columns (n) enumerates the different traces, and the matrix values are the probe differential transmission. Each column is as a vector $\mathbf{x}_k, k = 1\ldots n$, in a high-dimensional space, whose dimension is equal to the number of delay times. SVD is a linear transformation that factorizes the data matrix as $X = USV^T$ [42,49,50], where U is a matrix with the same dimensions as the dataset X. The columns of U are orthonormal vectors $\mathbf{u}_k$, called *left singular eigenvectors*. V is a square $n \times n$ matrix whose columns are constituted by orthonormal vectors $\mathbf{v}_k$, called *right singular eigenvectors*. S is a square diagonal $n \times n$ matrix whose values s_k are the eigenvalues associated with the eigenvectors called the *singular values*. Since the base vectors are much less than the space dimensions ($n \ll m$), we need as many singular values as left singular eigenvectors, i.e., the number of columns of U. By convention, the high-to-low sorting of eigenvalues, with the highest eigenvalue in the upper left corner of the S matrix, determines the ordering of the left singular eigenvectors. See SI, Section 4 for the SVD algorithm.

The left singular eigenvectors form a base onto which it is possible to project the experimental traces and reconstruct them as a weighted sum of projections. The weights needed for the reconstruction are given by the $n \times n$ *coordinate matrix* $M = SV^T$. The coefficients of M are the projections onto the left singular eigenvectors. The rows of M contains the coordinates of each measurement represented on this base. A useful way to reconstruct the experimental traces is expressed as $\mathbf{x}_k = \sum_{j=1}^{n} v_{jk} s_j \mathbf{u}_j = \sum_{j=1}^{n} m_{jk} \mathbf{u}_j$, where $m_{jk} = v_{jk} s_j$ are the elements of M. The elements of m_{jk} can be interpreted as the projections of the k^{th} trace onto the j^{th} eigenvector. Note that the singular values show the importance of the corresponding eigenvectors in reconstructing the dataset. Their ordering establishes a hierarchy. The first few eigenvectors account for an accurate approximate dataset reconstruction (dimensionality reduction).

The SVD decomposition guarantees that the approximation obtained using a limited number of projections to reconstruct the data matrix X is the best possible approximation in a least-square sense [49,42]. We use this low-rank approximation (or dimensionality reduction) to discriminate data and at the same time gain information on the dataset.

We use the entropy criterium to assess the smallest set of projections that give a good approximation and robust discrimination. The Shannon entropy E is defined through the singular values of the dataset as $0 \leqslant E = 1/\log(n) \sum_{k=1}^{n} p_k \log(1/p_k) \leqslant 1$, where $p_k = s_k^2 / \sum_{j=1}^{n} s_j^2$ [51]. Intuitively, Shannon entropy measures the *missing information* on a specific dataset. Low entropy means small differences between dataset elements, hinting at a dominant common backbone that explains the data variance. A high entropy shows the absence of similar features among the elements, hinting at a noise dominated dataset.

To assess the contribution of each eigenvector to the dataset entropy, we exclude (filter out) one singular value at a time in calculating the dataset entropy. Each filtered dataset is obtained by substituting zero for the singular value s_k in the diagonal matrix S when using the SVD reconstruction.

Fig. 5 a) reports the entropy calculation for the complete dataset ($k = 0$) and for 9 filtered dataset ($k = 1\ldots 9$), where the projection on the k^{th} eigenvector is excluded from the data reconstruction. Entropy increases by removing the first projection. Removing one of the remaining projections only slightly modifies the entropy value of the dataset. Clearly, the first projection ($k = 1$) carries most of the features common to all the elements, and reconstructing the dataset without its contribution leaves a quasi-random influence from the other eigenvectors and thus a high entropy for the reconstructed dataset. Instead, the projection on the eigenvectors with indexes $k = 2\ldots 9$, carry a noisy component equally distributed among them, and removing any one of them does not substantially modify the entropy value calculated for the complete dataset.

For discrimination purposes, similar features to all data are not useful, nor are noise dominated features. Thus, the best compromise appears to reconstruct data using two projections. The first one brings the dataset backbone and gives a small contribution to the entropy of the dataset. The second projection contributes the most to the entropy and has the highest singular value among the high entropy eigenvectors, see Fig. 5 b). This bi-dimensional low-rank approximation of a single trace $\mathbf{x}_k^r$, column vector of the low-rank matrix X^r, can be written as $\mathbf{x}_k^r = \sum_{j=1}^{2} v_{jk} s_j \mathbf{u}_j = \sum_{j=1}^{2} m_{jk} \mathbf{u}_j$, where $m_{jk} = v_{jk} s_j$ are the elements of the 2×9 projection matrix M. Each column of M gives the bidimensional projections over the base vectors $\mathbf{u}_j$ of the data $\mathbf{x}_k$. Each measurement is thus identified by a point in a two-dimensional space, whose coordinates are the elements of the coordinate matrix (m_{1k}, m_{2k}). In Fig. 6 we visualize the distribution of these points. In the scatter plot, these points form two clusters, evidenced as disjointed convex hulls. Each cluster contains points corresponding to the same nanodisk diameter. The convex hull of a cluster of points is the smallest convex polyhedron that contains all the cluster's points. In conclusion, SVD captures and analyzes the main differences in the spectra and perform robust and multivariate unsupervised discrimination with only two parameters.

Besides the primary scope of this work, i.e., the unsupervised and low-dimensional discrimination of different nanodisk batches, SVD allows the reconstruction of the average characteristic response of the identified clusters. The two largest singular values account for more than

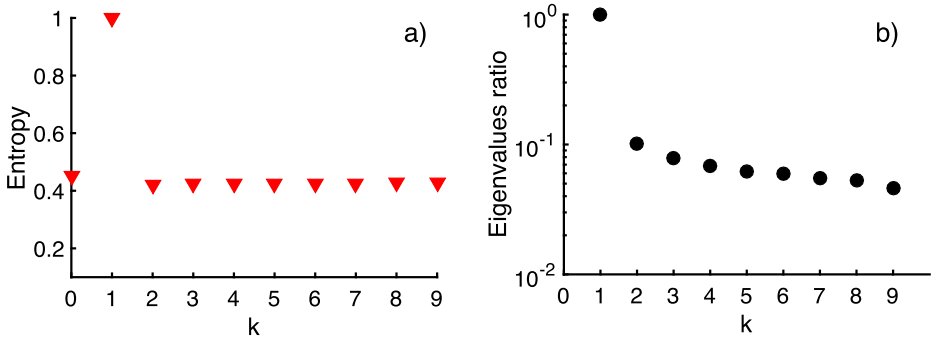

Fig. 5. Entropy associated to filtered datasets and the eigenvalues ratio (a) Entropy associated to the filtered dataset k, where the kth eigenvalue is removed from the computation. (b) The eigenvalues ratio s_k/s_1.

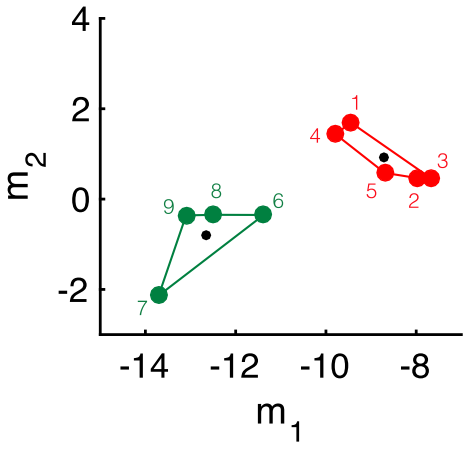

Fig. 6. Scatter plot representing the coordinates (m_{1k}, m_{2k}) of a specific trace k in the space spanned by the first two eigenvectors. The color code is the same as Fig. 2. Note that the 2D projections from disks of same diameter are grouped in separate clusters. The convex hulls of each group are shown. The black points mark the barycenter of the convex hull of each group.

70% of the total energy (see SI, Section 5) and thus constitute a sufficiently accurate low-rank representation of the original matrix X. Although there are other and more refined methods to decide the optimal low-rank representation of a matrix based on noise estimates (for example the L curve criterion [52], the optimal hard threshold [53]), we rely on the simpler criterion of total energy because adding higher singular values would only slightly improve the reconstruction quality, as the entropy analysis shows.

The average characteristic response can be obtained through the barycentric coordinates, represented by black points in Fig. 6. The barycentric traces are synthesized by the sum of the first two eigenvectors weighted by the barycentric coordinates of each cluster (dimensional reduction), see SI, Section 5. In Fig. 7 a) the barycentric traces are shown, for the 100 nm disks diameter ($i = 1$, red) and the 90 nm disks diameter ($i = 2$, green). The decay constants measure the thermal dissipation between the nanodisks and the substrate. Fig. 7 b) and c) show the characteristic oscillations due to the acoustic breathing modes of the disks, retrieved from the bi-exponentials residuals. These oscillations are well reproduced by a linear combination of two damped cosines at different frequencies, revealing that each nanodisk has at least two oscillation frequencies. The Fourier transforms of the residuals are reported in Fig. 7 d). The peaked structures evidenced in each cluster are compatible with those found in Fig. 2 b).

To demonstrate that the barycentric traces do provide reliable information, Fig. 8 reports all the parameters of the barycentric traces (diamonds) from the double exponential and double damped cosines fit and the same parameters obtained from the fits of *all* the experimental traces (circles) shown in Fig. 2 a). See SI, Section 3, for the fitting of the residuals. As a general observation, we note that the values extracted from the barycentric traces represent an approximate weighted average of that of the single traces, that show dispersion due to unavoidable experimental uncertainties. Significantly, this is true also for the fit of the barycentric residuals, which entails small-amplitude details that should be more difficult to reproduce in an approximate reconstruction.

Fig. 8 a) shows the values of the decay constants of the bi-exponential fits, characterized by a slow decay time τ_S, of the order of 1.5 ns, and a faster decay time τ_F, of the order of hundreds of ps. τ_F is comparable with the phonon–phonon scattering time reported in the literature [54–56], τ_S is due to the thermalization between the nanodisk and the sapphire substrate.

Fig. 8 b) shows the amplitudes A_S and A_F associated with the slow and fast decaying exponentials respectively. We note that A_S is the only parameter whose values form two distinct groups, one including 90 nm-diameter disks, the other 100 nm-diameter disks.

Fig. 8 c) displays the frequencies of the two damped cosines fits. The

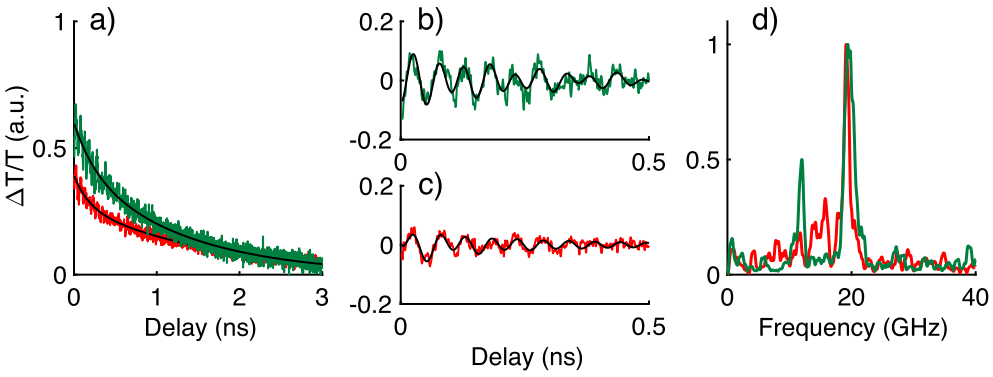

Fig. 7. The reconstructed representative traces of the clusters evidenced in Fig. 6, with the same color codes, and their analysis. (a) The traces obtained from the barycentric coordinates of the clusters using the first three eigenvectors. The black line is a bi-exponential fit function. (b) The residues of the biexponential fit for the 90 nm diameter disks. The black line is a fit with two damped cosines with different frequencies and damping. (c) Same as (b) for the 100 nm diameter disks. (d) The Fourier transform of the residues shown in (b) and (c).

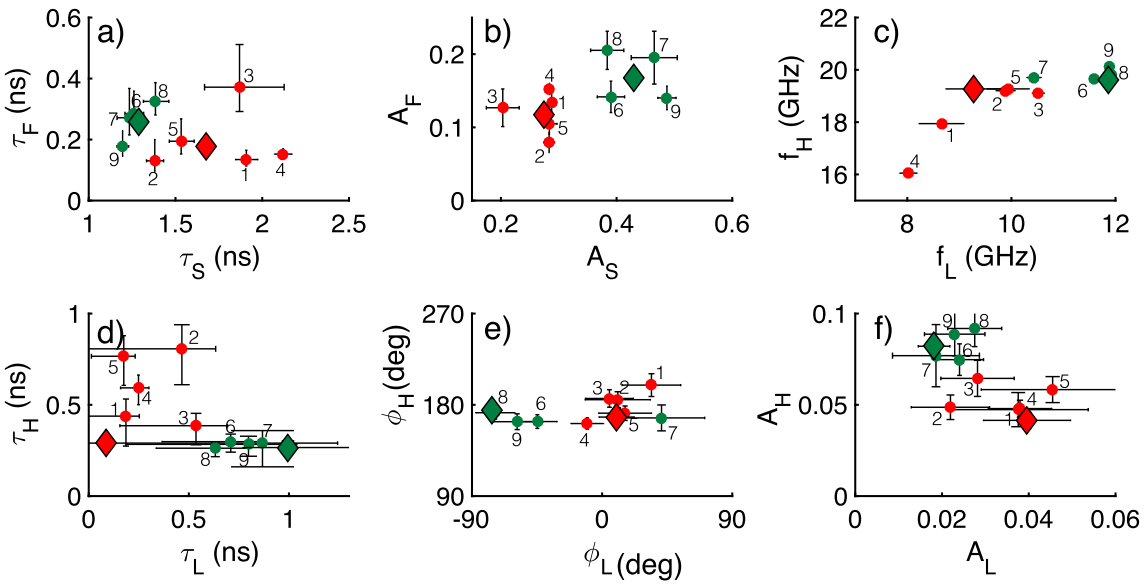

Fig. 8. Fitting parameters of all the traces shown in Fig. 2 (a) (circles) and of the barycentric traces (diamonds), with the same color codes. (a) Slow vs fast decay times (with error bars) as calculated in the double exponentials fits. (b) Amplitudes associated to slow and fast decay times (with error bars). (c) High and low frequencies of the two-damped cosines fit of the residues of the bi-exponential fit. (d) Damping times associated to the high and low frequencies of the two-damped cosines fit of the residues of the bi-exponential fit. (e) Phases associated to the high and low frequencies of the two-damped cosines fit of the residues of the bi-exponential fit. (f) Amplitudes associated to the high and low frequencies of the two-damped cosines fit of the residues of the bi-exponential fit.

values of the high frequency f_H and low frequency f_L from the barycentric traces correspond closely to the peaked structure observed in Fig. 7 d) and are identified with the acoustical oscillation modes of the disks after optical excitation.

In Fig. 8 d) the values of the damping constants in the cosine fits, associated with the high-frequency oscillation (τ_H) and with the low-frequency oscillation (τ_L) are shown. It is important to observe that the two clusters are characterized, on average, by different damping of the acoustical oscillations. The 90 nm diameter disks have damping times ($\tau_H = 265$ ps and $\tau_L = 1$ ns) longer than the corresponding oscillation periods ($1/f_H = 51$ ps and $1/f_L = 84$ ps respectively) while the 100 nm disks show very rapid damping for the low-frequency component ($\tau_L = 86$ ps), shorter than the corresponding oscillation period ($1/f_L = 108$ ps), and much longer decay time for the high-frequency component ($\tau_H = 290$ ps, $1/f_H = 52$ ps). This is why the oscillations in Fig. 7 c) are seen as a single oscillation frequency, without modulations, after roughly 150 ps. The rapid damping time associated with f_L is in agreement with the spectrally large structure peaked at 15 GHz observed in the Fourier transform of the residues for 100 nm diameter disks (Fig. 7 (d), red line), compared to the prominent and narrow peak at 12 GHz for the 90 nm diameter disks (Fig. 7 d), green line). The different dampings of oscillation frequencies are better appreciated in the calculation of the quality factor, roughly expressing the number of cycles before the oscillation amplitude dies out and being inversely proportional to the Fourier transform peak width. For the 90 nm diameter disks, the quality factors for the low and high-frequency oscillations are within a factor of two: $Q_L = 37$ and $Q_H = 16$. For the 100 nm diameter disks, the quality factor for the low-frequency oscillation is much lower than that associated with the high-frequency oscillation: $Q_L = 2$, $Q_H = 18$. These findings are in agreement with recent studies on the oscillation frequencies and damping of similar nanostructures [57].

Fig. 8 e) shows the phases associated with the low- and high-frequency damped cosines. Here we note that the barycentric traces of both 90 nm and 100 nm diameter disks are compatible with a phase near 180° (cos-like) for the high-frequency components (ϕ_H). The low-frequency components have a near-zero phase (ϕ_L) (cos-like) for the 100 nm disks and, on average, a $-90°$ phase shift for the 90 nm disks (sin-like).

Fig. 8 f) reports the amplitudes of the cosine fits, one associated with the high-frequency oscillation (A_H) and one with the low-frequency oscillation (A_L). The normalized peak amplitude has a relative transmission of the order of 1×10^{-5}. This implies that a normalized oscillation amplitude of 0.05 corresponds to a relative transmission of 5×10^{-7}.

This analysis shows that using the reconstructed traces from an extreme dimensional reduction, just two projections to reconstruct a trace, it is possible to retrieve the average parameters of the nanodisk thermo-mechanical dynamics and highlight the differences between the two nanodisk batches.

4. Conclusions

We have shown that it is possible to discriminate the experimental traces obtained from time-resolved photoacoustic nanoscopy performed on single metallic nanodisks with similar morphology and diameters differing by only 10%. The discrimination is accomplished by combining two different techniques: Hierarchical Binary Clustering and Singular Value Decomposition (SVD) analysis. These statistical tools have been applied to a well-known system like gold/titanium nanodisks, made by electronic beam lithography with a nominal diameter of 90 nm and 100 nm. The advantage is that such discrimination is easily obtained without previous knowledge of the physical system.

The Hierarchical Clustering method is based on the notion of distance between objects defined using an arbitrary metric, that classifies the similarity/dissimilarity between traces. The metric is not necessarily endowed with physical meaning, which limits the scope of the Clustering method to grouping and showing similarity/dissimilarity between traces and eventually isolates outliers.

The SVD analysis allows us to discriminate the traces based on a different approach. In this case, the projections of the experimental traces on the eigenvectors generate the coordinates of each trace in the space subtended by the eigenvectors base. We have reduced the data dimensions by projecting the original data into a subspace spanned by the two eigenvectors with the largest relative weight. The grouping of similar traces, in this case, is based on having similar projections. We note that the grouping of traces is not the only benefit of this

decomposition, eigenvectors shape also providing some physical insights. Specifically, the barycentric traces approximate the response of each group of nanodisks, giving insight into their main thermal and mechanical dynamics. We obtain information on the amplitude and the rate of decay of the accumulated energy in the nanodisks. The study of mechanical oscillations gives their periods and the corresponding relaxation times. In the near future, the SVD analysis will be implemented as a pre-analysis platform, having demonstrated that it can evidence those measures affected by casual or systematic errors.

The ASOPS technique used in this work is well adapted to be implemented in a microscope to study single nano-objects. The technique is inherently stable (absence of moving parts), yields high sensitivity, and allows a fast accumulation of pump–probe measurements with delays windows of the order of 10 ns in short times (one full trace per ms in the present case). Fast accumulation of traces enhances the statistics and reduces noise to a level not achievable with standard pump–probe techniques.

It is clear that these analysis techniques could be deployed as a rapid, effective and economical way of discriminating/testing nanostructures in industrial environments where the use of standard microscopies is not possible, not economical or not practical and a model to explain the transmissivity or reflectivity dynamics is not available.

Declaration of Competing Interest

The authors declare that they have no known competing financial interests or personal relationships that could have appeared to influence the work reported in this paper.

Acknowledgements

G.F. acknowledges financial support from the MIUR - PRIN 2017 grant in the frame of the aSTAR project (2017RKWTMY 003). C.G. and A.R. acknowledges financial support from MIUR through the PRIN 2017 program (Prot. 20172H2SC4 005). This work has been partially supported by the Università Cattolica del Sacro Cuore through D.3.1 and D.2.2 grants. F.B. acknowledges financial support from the MIUR - Futuro in Ricerca 2013 Grant in the frame of the ULTRANANO Project. F.B. acknowledges financial support from the IDEXLYON project Programme Investissements d'Avenir (ANR-16-IDEX-0005). M. G. acknowledges financial support from the CNR Joint Laboratories program 2019–2021, project SAC.AD002.026 (OMEN).

Appendix A. Supplementary material

Supplementary data associated with this article can be found, in the online version, at https://doi.org/10.1016/j.ultras.2021.106403.

References

[1] E. Cavaliere, G. Ferrini, P. Pingue, L. Gavioli, Fractal TiO_2 nanostructures by nonthermal laser ablation at ambient pressure, J. Phys. Chem. C 117 (44) (2013) 23305–23312.
[2] G. Celardo, D. Archetti, G. Ferrini, L. Gavioli, P. Pingue, E. Cavaliere, Evidence of diffusive fractal aggregation of TiO_2 nanoparticles by femtosecond laser ablation at ambient conditions, Mater. Res. Exp. 4 (1) (2017) 015013.
[3] E. Cavaliere, G. Benetti, G.L. Celardo, D. Archetti, P. Pingue, G. Ferrini, L. Gavioli, Aggregation and fractal formation of Au and TiO_2 nanostructures obtained by fs-pulsed laser deposition: experiment and simulation, J. Nanopart. Res. 19 (9) (2017) 311.
[4] S. Peli, E. Cavaliere, G. Benetti, M. Gandolfi, M. Chiodi, C. Cancellieri, C. Giannetti, G. Ferrini, L. Gavioli, F. Banfi, Mechanical properties of Ag nanoparticle thin films synthesized by supersonic cluster beam deposition, J. Phys. Chem. C 120 (8) (2016) 4673–4681.
[5] G. Benetti, C. Caddeo, C. Melis, G. Ferrini, C. Giannetti, N. Winckelmans, S. Bals, M. J. Van Bael, E. Cavaliere, L. Gavioli, et al., Bottom-up mechanical nanometrology of granular Ag nanoparticles thin films, J. Phys. Chem. C 121 (40) (2017) 22434–22441.
[6] C. Caddeo, C. Melis, A. Ronchi, C. Giannetti, G. Ferrini, R. Rurali, L. Colombo, F. Banfi, Thermal boundary resistance from transient nanocalorimetry: A multiscale modeling approach, Phys. Rev. B 95 (8) (2017) 085306.
[7] P.K. Jain, W. Qian, M.A. El-Sayed, Ultrafast electron relaxation dynamics in coupled metal nanoparticles in aggregates, J. Phys. Chem. B 110 (1) (2006) 136–142.
[8] S. Peli, A. Ronchi, G. Bianchetti, F. Rossella, C. Giannetti, M. Chiari, P. Pingue, F. Banfi, G. Ferrini, Optical and mechanical properties of streptavidin-conjugated gold nanospheres through data mining techniques, Scient. Rep. 10 (1) (2020) 1–13.
[9] F.S. Ligler, Perspective on optical biosensors and integrated sensor systems, Anal. Chem. 81 (2) (2009) 519–526, https://doi.org/10.1021/ac8016289.
[10] E.C. Dreaden, L.A. Austin, M.A. Mackey, M.A. El-Sayed, Size matters: gold nanoparticles in targeted cancer drug delivery, Therapeutic Deliv. 3 (4) (2012) 457–478.
[11] L. Paasonen, T. Laaksonen, C. Johans, M. Yliperttula, K. Kontturi, A. Urtti, Gold nanoparticles enable selective light-induced contents release from liposomes, J. Control. Release 122 (1) (2007) 86–93.
[12] X. Huang, M.A. El-Sayed, Gold nanoparticles: optical properties and implementations in cancer diagnosis and photothermal therapy, J. Adv. Res. 1 (1) (2010) 13–28.
[13] L.R. Hirsch, R.J. Stafford, J.A. Bankson, S.R. Sershen, B. Rivera, R. Price, J. D. Hazle, N.J. Halas, J.L. West, Nanoshell-mediated near-infrared thermal therapy of tumors under magnetic resonance guidance, Proc. Nat. Acad. Sci. 100 (23) (2003) 13549–13554.
[14] D. Nardi, E. Zagato, G. Ferrini, C. Giannetti, F. Banfi, Design of a surface acoustic wave mass sensor in the 100 GHz range, Appl. Phys. Lett. 100 (25) (2012) 253106, https://doi.org/10.1063/1.4729624.
[15] N. Stokes, A.M. McDonagh, M.B. Cortie, Preparation of nanoscale gold structures by nanolithography, Gold Bull. 40 (4) (2007) 310–320.
[16] A. Pimpin, W. Srituravanich, Review on micro- and nanolithography techniques and their applications, Eng. J. 16 (1) (2012) 37–56, https://doi.org/10.4186/ej.2012.16.1.37.
[17] G.N. Makarov, Laser applications in nanotechnology: nanofabrication using laser ablation and laser nanolithography, Phys. Usp. 56 (7) (2013) 643–682, https://doi.org/10.3367/UFNe.0183.201307a.0673.
[18] European technology platform for micro- and nano manufacturing (2020) [cited June 2020]. http://www.minamwebportal.eu/.
[19] B. Bhushan, Springer handbook of nanotechnology, Springer, 2010.
[20] P.W. Hawkes, J.C. Spence, Springer Handbook of Microscopy, Springer Nature (2019).
[21] T. Dehoux, O.B. Wright, R.L. Voti, Picosecond time scale imaging of mechanical contacts, Ultrasonics 50 (2) (2010) 197–201.
[22] P.M. Jais, D.B. Murray, R. Merlin, A.V. Bragas, Metal nanoparticle ensembles: tunable laser pulses distinguish monomer from dimer vibrations, Nano Lett. 11 (9) (2011) 3685–3689.
[23] T. Kelf, Y. Tanaka, O. Matsuda, E. Larsson, D.S. Sutherland, O. Wright, Ultrafast vibrations of gold nanorings, Nano Lett. 11 (9) (2011) 3893–3898.
[24] T. Stoll, P. Maioli, A. Crut, N. Del Fatti, F. Vallée, Advances in femto-nano-optics: ultrafast nonlinearity of metal nanoparticles, Eur. Phys. J. B 87 (11) (2014) 260.
[25] O. Matsuda, M.C. Larciprete, R.L. Voti, O.B. Wright, Fundamentals of picosecond laser ultrasonics, Ultrasonics 56 (2015) 3–20.
[26] K.M. Hoogeboom-Pot, E. Turgut, J.N. Hernandez-Charpak, J.M. Shaw, H. C. Kapteyn, M.M. Murnane, D. Nardi, Nondestructive measurement of the evolution of layer-specific mechanical properties in sub-10 nm bilayer films, Nano Lett. 16 (8) (2016) 4773–4778.
[27] D. Brick, V. Engemaier, Y. Guo, M. Grossmann, G. Li, D. Grimm, O.G. Schmidt, M. Schubert, V. Gusev, M. Hettich, et al., Interface adhesion and structural characterization of rolled-up GaAs/$In_{0.2}Ga_{0.8}As$ multilayer tubes by coherent phonon spectroscopy, Scient. Rep. 7 (1) (2017) 5385.
[28] M. Grossmann, M. Schubert, C. He, D. Brick, E. Scheer, M. Hettich, V. Gusev, T. Dekorsy, Characterization of thin-film adhesion and phonon lifetimes in Al/Si membranes by picosecond ultrasonics, New J. Phys. 19 (5) (2017) 053019.
[29] G. Beane, T. Devkota, B.S. Brown, G.V. Hartland, Ultrafast measurements of the dynamics of single nanostructures: a review, Rep. Prog. Phys. 82 (1) (2019) 016401.
[30] J. Mertz, Introduction to optical microscopy, Cambridge University Press, 2019.
[31] A. Diaspro, Nanoscopy and multidimensional optical fluorescence microscopy, CRC Press, 2010.
[32] F. Medeghini, R. Rouxel, A. Crut, P. Maioli, F. Rossella, F. Banfi, F. Vallée, N. Del Fatti, Signatures of small morphological anisotropies in the plasmonic and vibrational responses of individual nano-objects, J. Phys. Chem. Lett. 10 (2019) 5372.
[33] T. Ando, High-speed atomic force microscopy and its future prospects, Biophys. Rev. 10 (2) (2018) 285–292.
[34] G. Carleo, I. Cirac, K. Cranmer, L. Daudet, M. Schuld, N. Tishby, L. Vogt-Maranto, L. Zdeborová, Machine learning and the physical sciences, Rev. Mod. Phys. 91 (4) (2019) 045002.
[35] L. Xu, M. Rahmani, Y. Ma, D.A. Smirnova, K.Z. Kamali, F. Deng, Y.K. Chiang, L. Huang, H. Zhang, S. Gould, et al., Enhanced light–matter interactions in dielectric nanostructures via machine-learning approach, Adv. Photon. 2 (2) (2020) 026003.
[36] S. Peli, N. Nembrini, F. Damin, M. Chiari, C. Giannetti, F. Banfi, G. Ferrini, Discrimination of molecular thin films by surface-sensitive time-resolved optical spectroscopy, Appl. Phys. Lett. 107 (16) (2015) 163107, https://doi.org/10.1063/1.4934216.
[37] A. Bartels, R. Cerna, C. Kistner, A. Thoma, F. Hudert, C. Janke, T. Dekorsy, Ultrafast time-domain spectroscopy based on high-speed asynchronous optical sampling, Rev. Sci. Instrum. 78 (3) (2007) 035107.

[38] V.A. Stoica, Y.-M. Sheu, D.A. Reis, R. Clarke, Wideband detection of transient solid-state dynamics using ultrafast fiber lasers and asynchronous optical sampling, Opt. Exp. 16 (4) (2008) 2322–2335.
[39] D. Nardi, M. Travagliati, M.M. Murnane, H.C. Kapteyn, G. Ferrini, C. Giannetti, F. Banfi, Impulsively excited surface phononic crystals: a route toward novel sensing schemes, IEEE Sens. J. 15 (9) (2015) 5142–5150.
[40] M. Travagliati, D. Nardi, C. Giannetti, V. Gusev, P. Pingue, V. Piazza, G. Ferrini, F. Banfi, Interface nano-confined acoustic waves in polymeric surface phononic crystals, Appl. Phys. Lett. 106 (2) (2015) 021906.
[41] J.M. De Sá, Pattern recognition: concepts, methods, and applications, Springer-Verlag, 2001.
[42] I. Jolliffe, Principal component analysis, Wiley Online Library (2002).
[43] H. Barkhuijsen, R. De Beer, W. Bovee, D. Van Ormondt, Retrieval of frequencies, amplitudes, damping factors, and phases from time-domain signals using a linear least-squares procedure, J. Magn. Reson. (1969) 61 (3) (1985) 465–481.
[44] W.J. Tropf, M.E. Thomas, Aluminum oxide (Al_2O_3) revisited, in: Handbook of optical constants of solids, Elsevier, 1997, pp. 653–682.
[45] D.G. Cahill, S.-M. Lee, T.I. Selinder, Thermal conductivity of $\kappa-Al_2O_3 and \alpha-Al_2O_3$ wear-resistant coatings, J. Appl. Phys. 83 (11) (1998) 5783–5786.
[46] F. Banfi, F. Pressacco, B. Revaz, C. Giannetti, D. Nardi, G. Ferrini, F. Parmigiani, Ab initio thermodynamics calculation of all-optical time-resolved calorimetry of nanosize systems: Evidence of nanosecond decoupling of electron and phonon temperatures, Phys. Rev. B 81 (15) (2010) 155426.
[47] G.V. Hartland, Optical studies of dynamics in noble metal nanostructures, Chem. Rev. 111 (6) (2011) 3858–3887.
[48] C. Giannetti, F. Banfi, D. Nardi, G. Ferrini, F. Parmigiani, Ultrafast laser pulses to detect and generate fast thermomechanical transients in matter, IEEE Photon. J. 1 (1) (2009) 21–32.
[49] M.E. Wall, A. Rechtsteiner, L.M. Rocha, Singular value decomposition and principal component analysis, in: A practical approach to microarray data analysis, Springer, 2003, pp. 91–109.
[50] M. Tomoda, O. Matsuda, O.B. Wright, R. Li Voti, Tomographic reconstruction of picosecond acoustic strain propagation, Appl. Phys. Lett. 90 (4) (2007) 041114.
[51] O. Alter, P.O. Brown, D. Botstein, Singular value decomposition for genome-wide expression data processing and modeling, Proc. Nat. Acad. Sci. 97 (18) (2000) 10101–10106.
[52] C. Glorieux, R.L. Voti, J. Thoen, M. Bertolotti, C. Sibilia, Photothermal depth profiling: analysis of reconstruction errors, Inverse Prob. 15 (5) (1999) 1149.
[53] M. Gavish, D.L. Donoho, The optimal hard threshold for singular values is $4/\sqrt{3}$, IEEE Trans. Inf. Theory 60 (8) (2014) 5040–5053.
[54] S. Link, C. Burda, Z.L. Wang, M.A. El-Sayed, Electron dynamics in gold and gold–silver alloy nanoparticles: The influence of a nonequilibrium electron distribution and the size dependence of the electron–phonon relaxation, J. Chem. Phys. 111 (3) (1999) 1255–1264.
[55] J.H. Hodak, A. Henglein, G.V. Hartland, Electron-phonon coupling dynamics in very small (between 2 and 8 nm diameter) au nanoparticles, J. Chem. Phys. 112 (13) (2000) 5942–5947.
[56] S. Link, M.A. El-Sayed, Optical properties and ultrafast dynamics of metallic nanocrystals, Annu. Rev. Phys. Chem. 54 (1) (2003) 331–366.
[57] F. Medeghini, A. Crut, M. Gandolfi, F. Rossella, P. Maioli, F. Vallée, F. Banfi, N. Del Fatti, Controlling the quality factor of a single acoustic nanoresonator by tuning its morphology, Nano Lett. 18 (8) (2018) 5159–5166.